PHYSICS

Tracking ultrafast hot-electron diffusion in space and time by ultrafast thermomodulation microscopy

A. Block[1]*, M. Liebel[1], R. Yu[1], M. Spector[2], Y. Sivan[3], F. J. García de Abajo[1,4], N. F. van Hulst[1,4]*

Copyright © 2019 The Authors, some rights reserved; exclusive licensee American Association for the Advancement of Science. No claim to original U.S. Government Works. Distributed under a Creative Commons Attribution NonCommercial License 4.0 (CC BY-NC).

The ultrafast response of metals to light is governed by intriguing nonequilibrium dynamics involving the interplay of excited electrons and phonons. The coupling between them leads to nonlinear diffusion behavior on ultrashort time scales. Here, we use scanning ultrafast thermomodulation microscopy to image the spatiotemporal hot-electron diffusion in thin gold films. By tracking local transient reflectivity with 20-nm spatial precision and 0.25-ps temporal resolution, we reveal two distinct diffusion regimes: an initial rapid diffusion during the first few picoseconds, followed by about 100-fold slower diffusion at longer times. We find a slower initial diffusion than previously predicted for purely electronic diffusion. We develop a comprehensive three-dimensional model based on a two-temperature model and evaluation of the thermo-optical response, taking into account the delaying effect of electron-phonon coupling. Our simulations describe well the observed diffusion dynamics and let us identify the two diffusion regimes as hot-electron and phonon-limited thermal diffusion, respectively.

INTRODUCTION

Understanding light-induced charge-carrier transport is of vital importance in modern technological applications, such as solar cells, artificial photosynthesis, optical detectors, and heat management in optoelectronic devices (*1*–*4*). For example, the pathway of energy transfer in solar cells directly influences their energy conversion efficiency, as charge carriers need to diffuse toward extraction regions before being lost to other decay channels (*5*). Much active research on emerging sensitized or thin-film photovoltaics aims at engineering effective carrier transport while preventing hot-carrier loss (*6*, *7*). In modern optoelectronic devices, hot electrons are first accelerated by the incident field before they scatter and dissipate their energy on the nanometer to micrometer scale, eventually transferring excess energy either to the lattice or through Schottky junction harvesting (*8*–*10*). In the past, pump-probe techniques were widely used to study the ultrafast response of carrier and heat transport in different materials under optical excitation (*11*). While these time-resolved studies have uncovered numerous aspects of ultrafast carrier dynamics, the nanoscale spatial transport has remained largely unexplored. Direct real-space mapping to watch the carriers diffuse both in space and time is challenging. Recently, the combination of ultrafast spectroscopy and nanoimaging techniques, such as electron microscopy, x-ray diffraction, or near-field microscopy, has opened up new avenues to visualize microscopic transport (*12*–*14*). Unfortunately, these methods are invasive, require vacuum, or involve slow probe scanning. All-optical far-field pump-probe microscopy is an interesting alternative as it probes the system of interest in a perturbation-free manner while achieving both high temporal and spatial resolution (*15*, *16*). Using concepts of super-resolution and localization microscopy (*17*), the spatiotemporal dynamics can be resolved beyond the diffraction limit by precisely measuring the nanometer spatial changes of an initially excited, diffraction-limited region. Because of the relatively facile implementation, ultrafast microscopy is now emerging as an important tool for studying exciton diffusion in semiconductors, molecular solids, and two-dimensional (2D) materials (*18*–*21*). In this context, the ultrafast carrier diffusion dynamics in noble metals, such as gold, is of particular importance for heat management in nanoscale devices, as well as femtosecond laser ablation, but has thus far only been studied in the time domain (*22*–*30*).

In this work, we use novel ultrafast microscopy to gain insight into the complex nonequilibrium dynamics of hot electrons in gold. When a metal interacts with light, its electrons are excited above the Fermi level (Fig. 1A). These initially excited electrons trigger a cascade of cooling mechanisms that involve energy transfer between different metal subsystems, of which conduction electrons and lattice vibrations (phonons) are the dominant ones. The ultrafast thermal response is commonly described by considering the conduction band electrons and the ionic lattice as separate thermodynamic subsystems with distinct thermal properties, such as heat capacity and thermal conductivity (*31*). Since the heat capacity of the electrons is substantially smaller than that of the lattice, the electron subsystem quickly reaches a high temperature Fermi-Dirac distribution, which we refer to as "hot electrons," while the lattice stays close to ambient temperature under the excitation intensities considered here. The electrons subsequently cool and thermalize with the lattice within a few picoseconds. The electron relaxation and thermalization of the two subsystems are a direct result of an interplay between electron-phonon coupling and hot-electron diffusion (*27*). Purely time-resolved studies typically cannot separate these two contributions and have consistently neglected lateral heat flow (*25*, *27*), which becomes particularly important when considering nanoscale systems. Directly resolving hot-electron diffusion, a crucial step for understanding the ultrafast heat dynamics, has thus far not been possible because of a lack of spatiotemporal resolution (*27*–*29*).

Here, we address this shortcoming by interrogating thin gold films with our recently developed scanning ultrafast thermomodulation microscopy (SUTM) technique. We directly measure the spatiotemporal evolution of a locally induced hot-electron distribution on nanometer length scales with femtosecond resolution. Specifically, in our experiment, an optical pump pulse illuminates a thin gold film, thus creating hot carriers in the metal (Fig. 1B). We measure the subsequent

[1]ICFO–Institut de Ciencies Fotoniques, The Barcelona Institute of Science and Technology, 08860 Castelldefels (Barcelona), Spain. [2]Department of Physics, Ben-Gurion University of the Negev, 8410501 Be'er Sheva, Israel. [3]Unit of Electrooptics Engineering, Ben-Gurion University of the Negev, 8410501 Be'er Sheva, Israel. [4]ICREA–Institució Catalana de Recerca i Estudis Avançats, 08010 Barcelona, Spain.
*Corresponding author. Email: alexander.block@icfo.eu (A.B.); niek.vanhulst@icfo.eu (N.F.v.H.)

Downloaded from http://advances.sciencemag.org/ on May 12, 2019

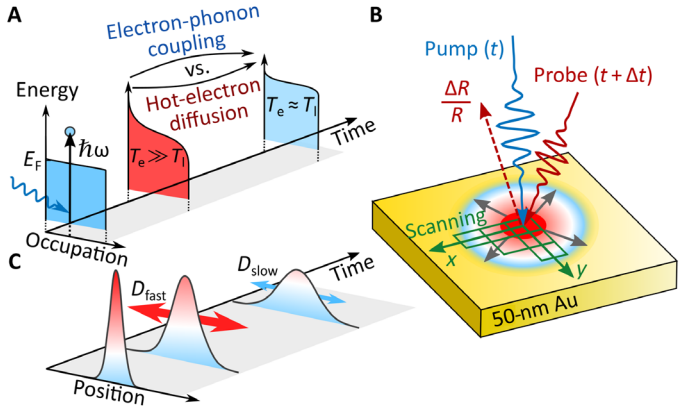

Fig. 1. Schematic description of scanning ultrafast thermomodulation microscopy. (**A**) The energy distribution of the conduction band electrons at ambient temperature is perturbed by optical excitation. It quickly evolves to a quasi-thermalized "hot-electron" Fermi-Dirac distribution with high electron temperature (T_e), while the lattice temperature (T_l) stays close to the ambient level. Subsequent cooling due to electron-phonon coupling and hot-carrier diffusion leads to thermal equilibrium between the electron and lattice subsystems. (**B**) An optical pump pulse illuminates a 50-nm thin gold film, thus inducing a local hot-electron distribution. The probe pulse measures the temperature-dependent transient reflectivity ($\Delta R/R$) as a function of both pump-probe time delay and pump-probe spatial offset. (**C**) We monitor the spatiotemporal evolution of the photoinduced $\Delta R/R$ spot size with 20-nm accuracy and 250-fs resolution to visualize and distinguish hot-electron diffusion and thermal (phonon-limited) diffusion.

thermal response of the metal by using a probe pulse that interrogates the sample at a well-defined time delay, Δt, with respect to the pump pulse. By spatially raster-scanning the probe beam relative to the stationary, tightly focused pump spot at each time delay, we obtain spatiotemporally resolved transient reflection ($\Delta R/R$) maps. In this experiment, spatial heat diffusion manifests itself as a broadening of the initially excited area, which is quantified with a nanometer accuracy, far beyond the diffraction limit, by accurate determination of the SUTM spatial response function (Fig. 1C). Considering the electron redistribution dynamics described above (Fig. 1A), we expect to identify distinct diffusion dynamics regimes, each dominated by a different diffusion mechanism, depending on the state of thermalization of the sample.

RESULTS

We image the light-induced thermal dynamics of a 50-nm thin gold film using SUTM. The sample is optically excited with a 450-nm (2.76 eV) pump pulse and interrogated with a 900-nm (1.38 eV) probe pulse, as outlined above (Fig. 1B). We focus the beams at the sample plane to spots of full width at half maximum (FWHM) of 0.6 and 0.9 μm, respectively, and record $\Delta R/R$ maps at different times after photoexcitation by varying the pump-probe delay between −5 and 30 ps.

Figure 2A shows transient reflection images, recorded at three different pump-probe time delays Δt for a fixed pump fluence F of 1.0 mJ/cm^2, which is well below the damage and ablation threshold of the metal (*32*). At $\Delta t = -2$ ps (i.e., when the probe interrogates the sample before photoexcitation by the pump), the $\Delta R/R$ response is negligible. Then, at $\Delta t = 0$ ps, a negative $\Delta R/R$ spot emerges around the pump beam position $x = y = 0$, with up to -10^{-4} contrast. Subsequently, at $\Delta t = 10$ ps, we observe a reduced response, as the signal has decayed. The negative sign of $\Delta R/R$ indicates that the heated area exhibits decreased reflection. The data were recorded with an integration time of 5 ms per pixel. To investigate the temporal decay dynamics, we spatially overlap the pump and probe beams ($x = y = 0$) and vary the time delay. Figure 2B shows the resulting trace. The transient reflection shows a negative step response with a 300-fs rise time, close to our instrument temporal resolution, followed by a biexponential decay with fast (1 ps) and slow (0.9 ns) components (see fig. S1). While these data contain information about the temporal carrier dynamics, the spatial diffusion information is provided by the $\Delta R/R$ maps of Fig. 2A. Therefore, we fit the central cross sections of the images with Gaussian functions (Fig. 2C). The FWHM increases by about 100 nm from 1.05 μm at Δt = 0 ps to 1.15 μm at Δt = 10 ps, a result that we attribute to spatial heat diffusion. The accuracy of this method is ultimately limited by the signal-to-noise ratio of the response function, which dictates how well the profiles can be fit. We observe an FWHM accuracy of about 20 nm.

We further investigate this evident diffusion behavior, as we want to track the rate at which it takes place during the thermalization process. Therefore, we proceed to record transient reflectivity line profiles over many pump-probe delays. Figure 3A shows a typical spatiotemporal dataset for $F = 1.0$ mJ/cm^2. We obtain an estimate of the time-dependent diffusion coefficient $D(t)$ in a first, semiquantitative manner by assuming the following relationship between the width (FWHM) and D for an initial Gaussian profile, which we adopt from a general treatment of diffusion problems (see note S1 for details) (*33*)

$$\frac{\partial \mathrm{FWHM}^2(t)}{\partial t} = 16\,(\ln 2)\,D(t) \qquad (1)$$

We extract the FWHM at each time delay by fitting Gaussian profiles to the $\Delta R/R$ maps, as previously explained, and plot the resulting temporal evolution of the squared width, FWHM^2, in Fig. 3B. We observe an initial fast spreading, revealed by an increase in FWHM^2, followed by a much slower broadening at longer time delays. The two diffusion regimes appear to correlate with the fast and slow temporal decay regimes of $\Delta R/R$. We estimate the initial and final diffusion coefficients by fitting lines to the curve in Fig. 3B (Eq. 1). Excluding the transition region, we restrict our fit to the Δt = 0 to 1 and 5 to 30 ps intervals, yielding $D_{fast} = 95$ cm^2/s and $D_{slow} = 1.1$ cm^2/s, respectively. We repeat the same procedure for multiple pump fluences and summarize the extracted coefficients, along with their standard errors, in the inset to Fig. 3B.

The above analysis provides a simple first measure to quantify diffusion. However, it relies on the assumption of a single diffusing profile and its proportionality to transient reflection while ignoring the underlying electron and phonon subsystems, as well as their individual thermal contributions to the reflection signal. Considering these (nonlinear) contributions to the dynamics, the asymptotic linear fitting is too simplistic. To fully understand the nature of the time-dependent diffusion mechanisms at work, particularly the transition between the two regimes of the observed spot broadening dynamics, it is necessary to model the response of the system more rigorously. Briefly, we model the spatiotemporal evolution of the pump-induced changes to the reflectivity of the sample in three basic steps (Fig. 4A). First, we calculate the electron and lattice temperature distributions in the gold film, $T_e(\mathbf{r},\Delta t)$ and $T_l(\mathbf{r},\Delta t)$ ($\mathbf{r} = x,y,z$), resolved in space and time, by means of a 3D two-temperature model (*30*, *31*). We then calculate the spatiotemporal dynamics of the gold film permittivity

Downloaded from http://advances.sciencemag.org/ on May 12, 2019

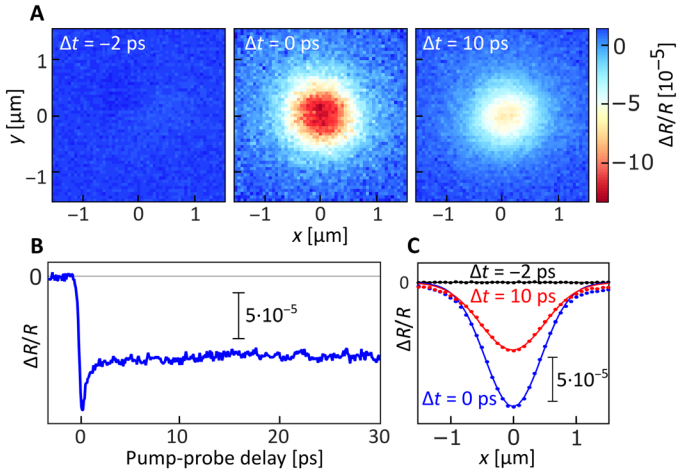

Fig. 2. Hot-electron dynamics. (**A**) Scanning ultrafast thermomodulation images of the gold film recorded by spatially scanning the probe beam (λ_{probe} = 900 nm) relative to a fixed pump beam position (λ_{pump} = 450 nm, centered at $x = y = 0$ in the image) for selected pump-probe delays. (**B**) Transient reflectivity dynamics for collinear pump and probe pulses, exhibiting two distinct exponential decay contributions with time constants of 1 ps and 0.9 ns, respectively. An offset at $\Delta t < 0$ has been subtracted from the data. (**C**) Spatial profiles (dots) and Gaussian fits (curves) for three selected pump-probe delays, extracted from (A) by cutting horizontal lines through the center of the spots ($y = 0$).

$\varepsilon(\mathbf{r},\Delta t)$, considering the effect of both temperatures on the Drude response. Last, we convert the permittivity to our observable, transient reflection $\Delta R/R(x,y,\Delta t)$ using the Fresnel equations (see Materials and Methods and fig. S2). This procedure allows us to directly compare the measured data to the predictions of our model for the spatiotemporal diffusion by Gaussian fitting of the resulting $\Delta R/R$ maps to obtain FWHM^2 as a function of Δt.

In more detail, we describe our system with a two-temperature model [i.e., in terms of two thermodynamic subsystems: the electrons and the lattice (*31*)]. We assume thermalization of the electron subsystem, as our temporal resolution of 250 fs cannot resolve the initial nonthermal stage right after photoexcitation. We model the 3D spatiotemporal temperatures in the gold film, $T_e(\mathbf{r},\Delta t)$ and $T_l(\mathbf{r},\Delta t)$, respectively, by considering the following coupled equations for the energy exchange between the gold electrons, the gold lattice, and the glass substrate, driven by a source $S(\mathbf{r},t)$ (the optical pump)

$$C_e(T_e)\frac{\partial T_e}{\partial t} = \nabla(k_e(T_e)\nabla T_e) - G(T_e - T_l) + S - S_{es} \quad (2a)$$

$$C_l\frac{\partial T_l}{\partial t} = \nabla(k_l\nabla T_l) + G(T_e - T_l) - S_{ls} \quad (2b)$$

$$C_s\frac{\partial T_s}{\partial t} = \nabla(k_s\nabla T_s) + S_{ls} + S_{es} \quad (2c)$$

where C_e/C_l (C_s) and k_e/k_l (k_s) are the volumetric heat capacity and thermal conductivity of the gold electron/lattice (glass substrate), respectively; G is the electron-phonon coupling coefficient; and S_{es} (S_{ls}) is an energy exchange parameter at the gold-glass interface for the gold electrons (lattice), as described in (*34*) (see the Supplementary Materials for more details and Materials and Methods for the parameter values).

We define the source term $S(\mathbf{r},t)$ for the energy absorbed from the pump pulse via its Gaussian spatial and temporal profiles (see details in note S2). We are careful to include the lateral (x,y) temperature gradient, as we are interested in the prediction of the model for the lateral heat flow out of the focal volume. A finite element method calculation yields the 3D spatiotemporal electron and lattice temperatures $T_e(\mathbf{r},\Delta t)$ and $T_l(\mathbf{r},\Delta t)$ for the sample geometry. The gold-air interface is taken to be at the $z = 0$ plane. The calculated evolution of the electron and lattice temperatures $T_{e/l}$ at $x = y = z = 0$ is shown in Fig. 4B. We observe a rapid increase in electron temperature to more than 1000 K and a subsequent cooling and thermalization with the lattice temperature at few tens of degrees above the ambient level of 293 K. Next, we calculate the spatiotemporal dependence of the gold film permittivity $\varepsilon(T_e(\mathbf{r},\Delta t),T_l(\mathbf{r},\Delta t))$ using a Drude model for the near-infrared probe wavelength (see Materials and Methods). The model includes electron-electron Umklapp scattering, electron-phonon scattering, and thermal lattice expansion in the calculation of the gold permittivity, which therefore depends on both T_e and T_l (see note S3). Then, the pump-induced complex permittivity is converted into transient reflectivity using the Fresnel coefficients for thin films as a function of lateral position (x,y) and time (Δt) to yield $\Delta R/R(\varepsilon(\mathbf{r},\Delta t))$, assuming a uniform permittivity across the film thickness (see note S4). The calculation actually predicts a higher $\Delta R/R$ contrast compared with experiment, possibly due to an overestimate of the absorbed power; however, this does not affect the width distributions. We account for the effect of the finite spatial extension of the probe pulse by convolving the resulting $\Delta R/R$ map with its measured, diffraction-limited width. Last, we analyze the predicted spatiotemporal evolution of $\Delta R/R$ by Gaussian fitting to the spatial cross sections, as described above for the experimental data. Figure 4C shows the calculated evolution of the squared width together with the experimental results for the three pump fluences under consideration. The comparison shows that the calculated evolution describes the experimental data well for both thermalization regimes, including the dependence on fluence. The relative difference Δ of the squared width between the full model and the experimental data lies below ±4% over the entire range of studied time delays.

DISCUSSION

Using scanning ultrafast thermomodulation microscopy, we have imaged the thermo-optical dynamics of gold films and identified two regimes of thermal diffusion dominated by hot electrons and lattice modes (phonons), respectively. Intuitively, the two observed regimes of heat diffusion may be understood from limiting cases of the two-temperature model. At early times, when $T_e \gg T_l$, the electron-lattice thermalization time can be estimated as $\tau_{e-ph} = C_e(T_e)/G$, and the hot-electron-dominated diffusion can be estimated as $D_{fast} = k_e/C_e$, as previously predicted (*22*). In the long term, after thermalization of the electrons and the lattice ($T_e \approx T_l$), the two-temperature model simplifies to a diffusion equation with $D_{slow} = (k_e + k_l)/(C_e + C_l) \approx k_e/C_l$. This is the well-known thermal diffusivity of gold (*35*). Inserting the values of electron-phonon coupling constant, heat capacity, and thermal conductivity leads to τ_{e-ph} = 1 to 3 ps (for T_e = 300 to 1000 K), D_{fast} = 152 cm^2/s, and D_{slow} = 1.36 cm^2/s. However, $D_{fast} = k_e/C_e$, also shown as a gray dashed line in Fig. 4C, only serves as a preliminary estimation, which overestimates the values observed by our spatiotemporal imaging (see also inset to Fig. 3B). Obviously, the delaying effect of electron-phonon coupling on the diffusion dynamics needs to be taken into account. Modeling the full dynamics from absorption through

Downloaded from http://advances.sciencemag.org/ on May 12, 2019

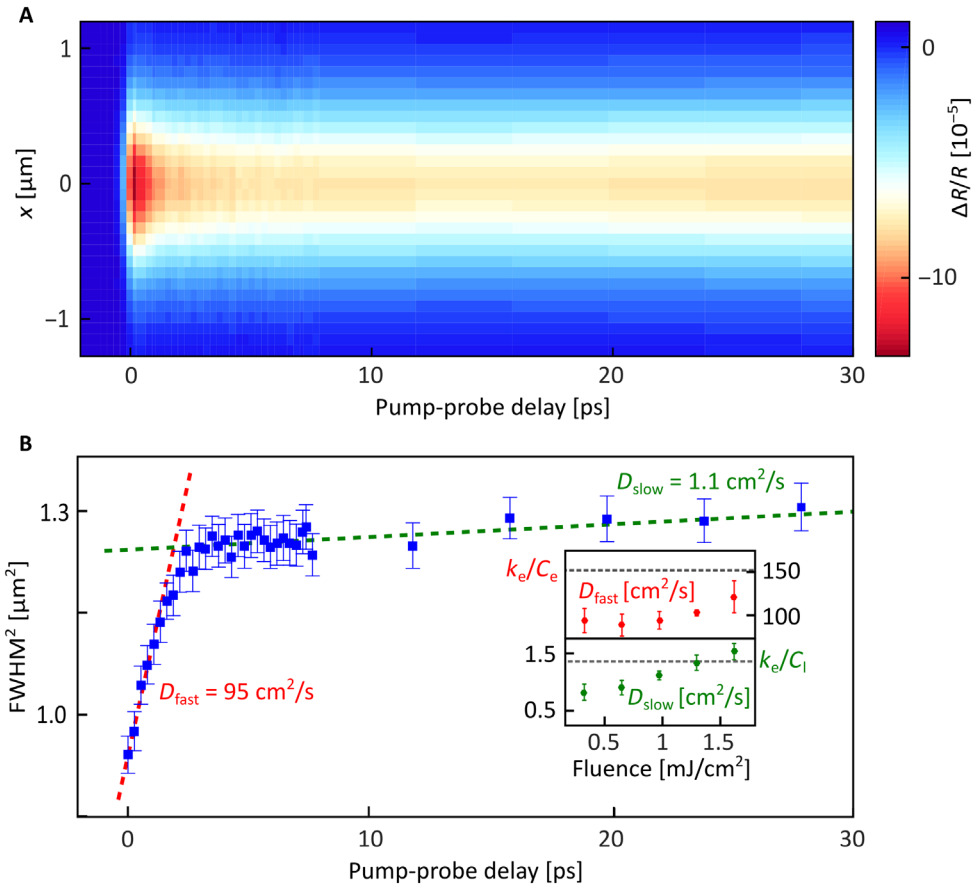

Fig. 3. Two-step diffusion dynamics. (**A**) Spatiotemporal dynamics of the transient reflection signal $\Delta R/R$. We scan the probe beam over the pump beam (1D scan across spot center, vertical axis) as a function of pump-probe delay (horizontal axis) at a pump fluence of 1.0 mJ/cm^2. The offset at $\Delta t < 0$ has been subtracted from the data. (**B**) Squared-width evolution of the $\Delta R/R$ profile, extracted by Gaussian fitting to the spatial profile at each pump-probe delay (symbols). The error bars show the 68% confidence intervals of the Gaussian fits. We extract the initial and final diffusion coefficients by fitting slopes in the two regions (dashed lines) and comparing to Eq. 1. We find fast diffusion of D_{fast} = 95 cm^2/s within the first few picoseconds, followed by slower diffusion (D_{slow} = 1.1 cm^2/s) after >5 ps. The inset shows the extracted diffusion coefficients for pump fluences in the range of 0.3 to 1.6 mJ/cm^2, along with the ratio of electron thermal conductivity k_e and electron (lattice) heat capacity C_e (C_l).

electron-lattice thermalization to spatiotemporal permittivity dynamics allows us to predict the evolution of the spatial width of $\Delta R/R$, resulting in good quantitative agreement with the experimentally determined time-dependent diffusion. In particular, it illustrates how the elevated temperature of the conduction band electrons correlates with a fast carrier diffusion and how both electron-phonon coupling and hot-electron diffusion contribute to the transition between the two mentioned regimes. We note that our model relies purely on reported material constants and has no free adjustable parameters (see Materials and Methods). In addition, the dependence of the calculated width evolution on the laser fluence agrees well with the experimental data.

In the transition regime, around 5-ps time delay, we predict a subtle decrease of FWHM, which lies within the uncertainty of the experimental data. In fact, the two-temperature model predicts a substantial decrease of FWHM for the electron temperature distribution (i.e., apparent negative diffusion) in this transition regime. The effect is less visible after conversion to our observable, $\Delta R/R$, both experimentally and in simulation, presumably because of the influence of the lattice temperature in the crossover regime.

Recent experiments have studied the effects of nonthermal electron distributions, as well as a transition from ballistic to diffusive electron transport (*23*, *36*). It will be interesting to study these effects in real space with SUTM at higher temporal resolution.

In summary, we have tracked thermally induced diffusion in a thin gold film from absorption to thermalization in time and space with femtosecond and nanometer resolution. We resolve a transition from hot-electron to phonon-limited diffusion. We interpret the electronic and phononic cooling regimes with the help of full two-temperature and thermo-optical modeling. The predicted dynamics agree well with the experimental observations. The insight gained on hot-carrier dynamics from direct spatiotemporal imaging is crucial to understand the interplay of electrons and phonons in ultrafast nanoscale photonics and thus to design nanoscale thermal management in nano-optoelectronic devices, such as phase-change memory devices and heat-assisted magnetic recording heads. In particular, the control of heat exchange between the electron and lattice systems is important in device functionality. More generally, the excess energy of hot electrons finds applications in an increasingly wide range of systems, such as thermoelectric devices, broadband photodetectors, efficient solar cells, and even plasmon-enhanced photochemistry. Here, we have applied our method to gold, the "gold" standard for many such applications of electron heat. Certainly, ultrafast thermomodulation

Downloaded from http://advances.sciencemag.org/ on May 12, 2019

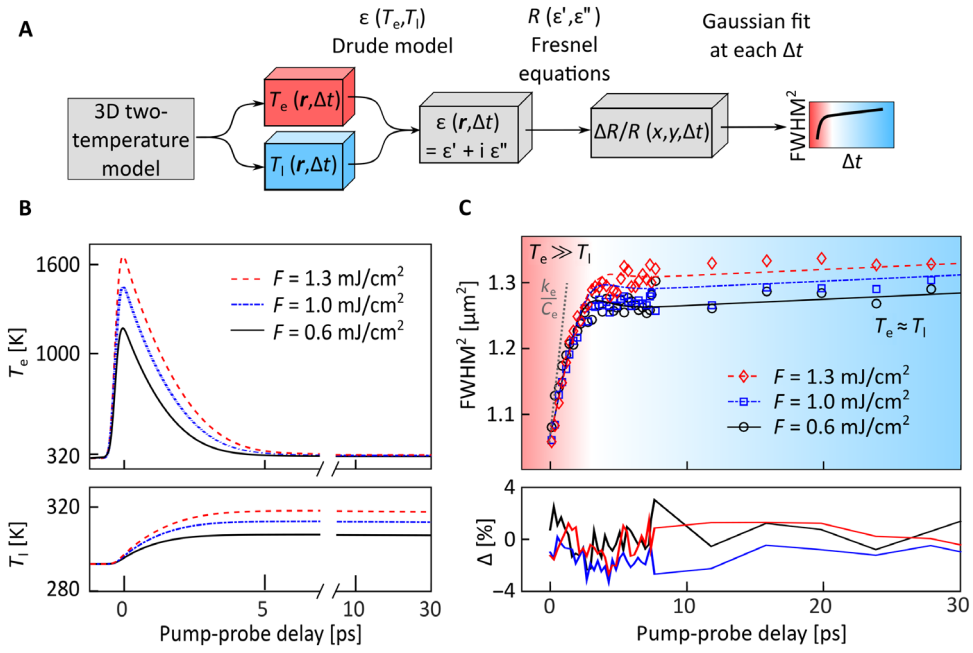

Fig. 4. Theoretical modeling and identification of different diffusion regimes. (**A**) We simulate the spatiotemporal evolution of the optically excited gold film with a full 3D-space two-temperature model. We obtain the temperature-dependent complex permittivity from the calculated spatiotemporal electron and lattice temperature maps, including the thermal dependence of electron-electron and electron-phonon scattering, as well as thermal expansion of the lattice. We then calculate $\Delta R/R(x,y,\Delta t)$ using the thin-film Fresnel equations and extract its spatial dynamics using the same Gaussian fitting as in the experimental data analysis. (**B**) Predicted temporal evolution of the electron (top) and lattice (bottom) temperatures at the beam center for the three pump fluences used in the experiment. (**C**) Theoretical (curves) and experimental (symbols) evolution of the squared width of $\Delta R/R$ for different pump fluences F (top). In accordance with Fig. 3B, we identify a fast diffusion regime at high electron temperatures, within the first few picoseconds, followed by a thermalized regime (>5 ps) dominated by phonon-limited transport, with orders-of-magnitude lower diffusivity. The initial slope for a diffusivity of $D = k_e/C_e$ is shown for comparison. Bottom: Difference Δ between the data and the full model calculation.

microscopy is equally suitable to study a vast range of other materials and systems in the future.

MATERIALS AND METHODS

Experimental details

The sample was fabricated by thermal evaporation of 50 nm of gold onto a cleaned glass coverslip. The laser source was a Ti:Sapphire oscillator (Mira 900, Coherent) emitting at 900-nm wavelength with a repetition rate of 76 MHz and a 150-fs pulse duration. We frequency-doubled the laser using a BBO crystal to create the 450-nm pump beam. We compressed the pump and probe pulses individually with two prism compressors made of fused silica and SF10 glass, respectively. We characterized the temporal resolution of the entire imaging system at the sample plane as 250 fs via the 10 to 90% cross-correlation rise time of a transient absorption signal of a graphene sample. Both beams were focused onto the sample with a 40×/0.6 numerical aperture objective lens (LUC Plan FLN, Olympus). We measured the beam profile at the sample plane by scanning a line edge of the gold film through the beam. We minimized and overlapped the pump and the probe beam foci in the sample plane by iterative (de-)collimation and beam profiling, resulting in values of $FWHM_{pump} = 0.6$ μm and $FWHM_{probe} = 0.9$ μm at the same z position. We scanned the probe beam over the pump with a two-axis mirror galvanometer system (GVS012, Thorlabs). We modulated the pump beam with an optical chopper (Model 3501, New Focus) at 6.4 kHz and recorded transient reflection by long-wave pass filtering (585ALP and 740AELP, Omega Optical) of only the probe beam onto a balanced photodiode (PDB450C, Thorlabs) and lock-in amplification (SR830, Stanford Research Systems). A sketch of the setup is shown in fig. S3.

Two-temperature model, finite element method implementation

For the two-temperature model calculations (Eq. 2), we used the following parameters and scaling laws: the electronic volumetric heat capacity of gold (*27*) $C_e(T_e) = \gamma T_e$, with $\gamma = 71\ \mathrm{Jm^{-3}\,K^{-2}}$; the electronic thermal conductivity of gold (*27*) $k_e(T_e,T_l) = k_0 T_e/T_l$, with $k_0 = 317\ \mathrm{Wm^{-1}\,K^{-1}}$; the lattice heat capacity and thermal conductivity of gold (*37*, *38*) $C_l = 2.45 \times 10^6\ \mathrm{Jm^{-3}\,K^{-1}}$ and $k_l = 2.6\ \mathrm{Wm^{-1}\,K^{-1}}$, respectively; the electron-phonon coupling constant (*39*) $G = 2.2 \times 10^{16}\ \mathrm{Wm^{-3}\,K^{-1}}$; and the heat capacity and thermal conductivity of glass (*40*) $C_s = 1.848 \times 10^6\ \mathrm{Jm^{-3}\,K^{-1}}$ and $k_s = 0.8\ \mathrm{Wm^{-1}\,K^{-1}}$, respectively (see note S2 for further details).

Thermo-optical response calculation

We modeled the complex permittivity at the infrared probe wavelength with a Drude model permittivity (*41*)

$$\varepsilon = \varepsilon_\infty - \frac{{\omega_p}^2(T_l)}{\omega(\omega + i\gamma_{re}(T_e, T_l))}$$

Here, $\varepsilon_\infty = 9.5$ is the high-frequency permittivity (*41*). The plasma frequency ω_p depends on the lattice temperature T_l due to volume expansion affecting the free conduction band electron density n_e. Namely, $\omega_p(T_l) = \sqrt{(e^2/\varepsilon_0 m_{eff}) \times n_e(T_0)/(1 + \beta\Delta T_l)}$, where $\beta = 4.23 \times 10^{-5}\ \mathrm{K^{-1}}$ is the

Downloaded from http://advances.sciencemag.org/ on May 12, 2019

thermal expansion coefficient (*42*), $n_e(T_0) = 5.9 \times 10^{22}$ cm^{-3} is the unperturbed density (*42*), $m_{eff} \approx m_e$ is the effective electron mass, ε_0 is the vacuum permittivity, and m_e and e and are the elementary charge and mass, respectively. Further, γ_{re} represents the total rate of relaxation collisions that conserve momentum and energy of the electron subsystem, given by $\gamma_{re}(T_e, T_l) = \gamma_{e-ph}(T_l) + \gamma_{e-e}^{Um}(T_e)$, where γ_{e-ph} is the electron-phonon collision rate, depending on the lattice temperature as $\gamma_{e-ph}(T_l) = BT_l$, and γ_{e-e}^{Um} is the Umklapp electron-electron collision rate, depending on T_e as $\gamma_{e-e}^{Um}(T_e) = \Delta^{(Um)} A T_e^2$, with $A = 1.7 \times 10^7$ K^{-2} s^{-1}, $B = 1.45 \times 10^{11}$ K^{-1} s^{-1}, and $\Delta^{Um} = 0.77$ (see note S3 and fig. S2) (*43*, *44*).

SUPPLEMENTARY MATERIALS

Supplementary material for this article is available at http://advances.sciencemag.org/cgi/content/full/5/5/eaav8965/DC1

Note S1. General diffusion model
Note S2. Two-temperature model
Note S3. Thermo-optical response
Note S4. Calculation of the transient reflectivity
Fig. S1. Long-time dynamics of $\Delta R/R$.
Fig. S2. Scheme of thermo-optical calculations.
Fig. S3. Schematic of the SUTM setup.
Fig. S4. Different contributions to the thermo-optical response.
References (*45*–*57*)

REFERENCES AND NOTES

1. A. Polman, H. A. Atwater, Photonic design principles for ultrahigh-efficiency photovoltaics. *Nat. Mater.* **11**, 174–177 (2012).
2. Y. Tachibana, L. Vayssieres, J. R. Durrant, Artificial photosynthesis for solar water-splitting. *Nat. Photonics* **6**, 511–518 (2012).
3. A. O. Goushcha, B. Tabbert, On response time of semiconductor photodiodes. *Opt. Eng.* **56**, 097101 (2017).
4. N. Han, T. V. Cuong, M. Han, B. D. Ryu, S. Chandramohan, J. B. Park, J. H. Kang, Y.-J. Park, K. B. Ko, H. Y. Kim, H. K. Kim, J. H. Ryu, Y. S. Katharria, C.-J. Choi, C.-H. Hong, Improved heat dissipation in gallium nitride light-emitting diodes with embedded graphene oxide pattern. *Nat. Commun.* **4**, 1452–1458 (2013).
5. J. A. Bartelt, D. Lam, T. M. Burke, S. M. Sweetnam, M. D. McGehee, Charge-carrier mobility requirements for bulk heterojunction solar cells with high fill factor and external quantum efficiency >90%. *Adv. Energy Mater.* **5**, 1500577 (2015).
6. M. Grätzel, Dye-sensitized solar cells. *J. Photochem. Photobiol. C Photochem. Rev.* **4**, 145–153 (2003).
7. A. J. Nozik, Quantum dot solar cells. *Phys. E Low-Dimensional Syst. Nanostructures.* **14**, 115–120 (2002).
8. M. L. Brongersma, N. J. Halas, P. Nordlander, Plasmon-induced hot carrier science and technology. *Nat. Nanotechnol.* **10**, 25–34 (2015).
9. J. R. M. Saavedra, A. Asenjo-Garcia, F. J. García De Abajo, Hot-electron dynamics and thermalization in small metallic nanoparticles. *ACS Photonics* **3**, 1637–1646 (2016).
10. E. W. McFarland, J. Tang, A photovoltaic device structure based on internal electron emission. *Nature* **421**, 616–618 (2003).
11. J. Cabanillas-Gonzalez, G. Grancini, G. Lanzani, Pump-probe spectroscopy in organic semiconductors: Monitoring fundamental processes of relevance in optoelectronics. *Adv. Mater.* **23**, 5468–5485 (2011).
12. E. Najafi, V. Ivanov, A. Zewail, M. Bernardi, Super-diffusion of excited carriers in semiconductors. *Nat. Commun.* **8**, 15177 (2017).
13. K. J. Gaffney, H. N. Chapman, Imaging atomic structure and dynamics with ultrafast X-ray scattering. *Science* **316**, 1444–1448 (2007).
14. V. Emiliani, T. Guenther, C. Lienau, R. Nötzel, K. H. Ploog, Femtosecond near-field spectroscopy: Carrier relaxation and transport in single quantum wires. *J. Microsc.* **202**, 229–240 (2001).
15. E. M. Grumstrup, M. M. Gabriel, E. E. M. Cating, E. M. Van Goethem, J. M. Papanikolas, Pump–probe microscopy: Visualization and spectroscopy of ultrafast dynamics at the nanoscale. *Chem. Phys.* **458**, 30–40 (2015).
16. D. Davydova, A. de la Cadena, D. Akimov, B. Dietzek, Transient absorption microscopy: Advances in chemical imaging of photoinduced dynamics. *Laser Photonics Rev.* **10**, 62–81 (2016).
17. E. Betzig, G. H. Patterson, R. Sougrat, O. Wolf Lindwasser, S. Olenych, J. S. Bonifacino, M. W. Davidson, J. Lippincott-Schwartz, H. F. Hess, Imaging intracellular fluorescent proteins at nanometer resolution. *Science* **313**, 1642–1645 (2006).
18. B. A. Ruzicka, L. K. Werake, H. Samassekou, H. Zhao, Ambipolar diffusion of photoexcited carriers in bulk GaAs. *Appl. Phys. Lett.* **97**, 262119 (2010).
19. Y. Wan, T. Zhu, S. Yan, J. Johnson, L. Huang, Cooperative singlet and triplet exciton transport in tetracene crystals visualized by ultrafast microscopy. *Nat. Chem.* **7**, 785–792 (2015).
20. F. Ceballos, H. Zhao, Ultrafast laser spectroscopy of two-dimensional materials beyond graphene. *Adv. Funct. Mater.* **27**, 1604509 (2017).
21. Z. Guo, Y. Wan, M. Yang, J. Snaider, K. Zhu, L. Huang, Long-range hot-carrier transport in hybrid perovskites visualized by ultrafast microscopy. *Science* **356**, 59–62 (2017).
22. R. W. Schoenlein, W. Z. Lin, J. G. Fujimoto, G. L. Eesley, Femtosecond studies of nonequilibrium electronic processes in metals. *Phys. Rev. Lett.* **58**, 1680–1683 (1987).
23. S. D. Brorson, J. G. Fujimoto, E. P. Ippen, Femtosecond electronic heat-transport dynamics in thin gold films. *Phys. Rev. Lett.* **59**, 1962–1965 (1987).
24. W. S. Fann, R. Storz, H. W. K. Tom, J. Bokor, Direct measurement of nonequilibrium electron-energy distributions in subpicosecond laser-heated gold films. *Phys. Rev. Lett.* **68**, 2834–2837 (1992).
25. C.-K. Sun, F. Vallée, L. H. Acioli, E. P. Ippen, J. G. Fujimoto, Femtosecond-tunable measurement of electron thermalization in gold. *Phys. Rev. B.* **50**, 15337–15348 (1994).
26. S.-S. Wellershoff, J. Hohlfeld, J. Güdde, E. Matthias, The role of electron–phonon coupling in femtosecond laser damage of metals. *Appl. Phys. A.* **69**, S99–S107 (1999).
27. M. Bonn, D. N. Denzler, S. Funk, M. Wolf, S.-S. Wellershoff, J. Hohlfeld, Ultrafast electron dynamics at metal surfaces: Competition between electron–phonon coupling and hot-electron transport. *Phys. Rev. B.* **61**, 1101–1105 (2000).
28. N. Del Fatti, C. Voisin, M. Achermann, S. Tzortzakis, D. Christofilos, F. Vallée, Nonequilibrium electron dynamics in noble metals. *Phys. Rev. B.* **61**, 16956–16966 (2000).
29. J. Hohlfeld, S.-S. Wellershoff, J. Güdde, U. Conrad, V. Jähnke, E. Matthias, Electron and lattice dynamics following optical excitation of metals. *Chem. Phys.* **251**, 237–258 (2000).
30. B. Rethfeld, D. S. Ivanov, M. E. Garcia, S. I. Anisimov, Modelling ultrafast laser ablation. *J. Phys. D Appl. Phys.* **50**, 193001 (2017).
31. S. I. Anisimov, B. L. Kapeliovich, T. L. Perel'man, Electron emission from metal surfaces exposed to ultrashort laser pulses. *J. Exp. Theor. Phys.* **66**, 375–377 (1974).
32. B. J. Demaske, V. V. Zhakhovsky, N. A. Inogamov, I. I. Oleynik, Ablation and spallation of gold films irradiated by ultrashort laser pulses. *Phys. Rev. B.* **82**, 064113 (2010).
33. J. Crank, *The Mathematics of Diffusion* (Oxford Univ. Press, 1975).
34. L. Meng, R. Yu, M. Qiu, F. J. García de Abajo, Plasmonic nano-oven by concatenation of multishell photothermal enhancement. *ACS Nano* **11**, 7915–7924 (2017).
35. J. A. King, *Materials Handbook for Hybrid Microelectronics* (Artech House, 1988).
36. T. Juhasz, H. E. Elsayed-Ali, G. O. Smith, C. Suárez, W. E. Bron, Direct measurements of the transport of nonequilibrium electrons in gold films with different crystal structures. *Phys. Rev. B.* **48**, 15488–15491 (1993).
37. C. Kittel, *Introduction to Solid State Physics* (Wiley, ed. 8, 2005).
38. Y. Wang, Z. Lu, X. Ruan, First principles calculation of lattice thermal conductivity of metals considering phonon-phonon and phonon–electron scattering. *J. Appl. Phys.* **119**, 225109 (2016).
39. J. Bin Lee, K. Kang, S. H. Lee, Comparison of theoretical models of electron–phonon coupling in thin gold films irradiated by femtosecond pulse lasers. *Mater. Trans.* **52**, 547–553 (2011).
40. A. Sousa-Castillo, Ó. Ameneiro-Prieto, M. Comesaña-Hermo, R. Yu, J. M. Vila-Fungueiriño, M. Pérez-Lorenzo, F. Rivadulla, F. J. García de Abajo, M. A. Correa-Duarte, Hybrid plasmonic nanoresonators as efficient solar heat shields. *Nano Energy* **37**, 118–125 (2017).
41. P. B. Johnson, R. W. Christy, Optical constants of the noble metals. *Phys. Rev. B.* **6**, 4370–4379 (1972).
42. N. W. Ashcroft, N. D. Mermin, *Solid State Physics* (Harcourt Inc., 1976).
43. A. N. Smith, P. M. Norris, Influence of intraband transitions on the electron thermoreflectance response of metals. *Appl. Phys. Lett.* **78**, 1240–1242 (2001).
44. J.-S. G. Bouillard, W. Dickson, D. P. O'Connor, G. A. Wurtz, A. V. Zayats, Low-temperature plasmonics of metallic nanostructures. *Nano Lett.* **12**, 1561–1565 (2012).
45. J. Zhang, Y. Chen, M. Hu, X. Chen, An improved three-dimensional two-temperature model for multi-pulse femtosecond laser ablation of aluminum. *J. Appl. Phys.* **117**, 063104 (2015).
46. P.-T. Shen, Y. Sivan, C.-W. Lin, H.-L. Liu, C.-W. Chang, S.-W. Chu, Temperature- and roughness- dependent permittivity of annealed/unannealed gold films. *Opt. Express* **24**, 19254–19263 (2016).
47. H. Reddy, U. Guler, A. V. Kildishev, A. Boltasseva, V. M. Shalev, Temperature-dependent optical properties of gold thin films. *Opt. Mater. Express.* **6**, 2776–2802 (2016).
48. V. Z. Kresin, G. O. Zaĭtsev, Temperature dependence of the electron specific heat and effective mass. *Sov. J. Exp. Theor. Phys.* **47**, 983 (1978).
49. R. E. Peierls, *Quantum Theory of Solids* (Oxford Univ. Press, 2001).

Downloaded from http://advances.sciencemag.org/ on May 12, 2019

50. M. Kaveh, N. Wiser, Electron–electron scattering in conducting materials. *Adv. Physiol. Educ.* **33**, 257–372 (1984).
51. D. Pines, P. Nozières, *The Theory of Quantum Liquids* (W.A. Benjamin, 1966).
52. R. H. M. Groeneveld, R. Sprik, A. Lagendijk, Femtosecond spectroscopy of electron–electron and alectron-phonon energy relaxation in Ag aund Au. *Phys. Rev. B.* **51**, 11433–11445 (1995).
53. R. N. Gurzhi, On the theory of the infrared absorptivity of metals. *Sov. Phys. JETP.* **6**, 506–512 (1958).
54. L. D. Landau, E. M. Lifshitz, *Statistical Physics Part I* (Pergamon Press, 1980).
55. L. Burakovsky, D. L. Preston, Analytic model of the Grüneisen parameter all densities. *J. Phys. Chem. Solids.* **65**, 1581–1587 (2004).
56. O. A. Yeshchenko, I. S. Bondarchuk, V. S. Gurin, I. M. Dmitruk, A. V. Kotko, Temperature dependence of the surface plasmon resonance in gold nanoparticles. *Surf. Sci.* **608**, 275–281 (2013).
57. M. Born, E. Wolf, *Principles of Optics* (Cambridge Univ. Press, 2009).

Acknowledgments: We thank P. Woźniak for helpful discussions while preparing the manuscript. **Funding:** A.B. acknowledges financial support from the International PhD fellowship program "la Caixa"–Severo Ochoa. This project is financially supported by the European Commission (ERC Advanced Grants 670949-LightNet and 789104-eNANO), Spanish Ministry of Economy ("Severo Ochoa" program for Centres of Excellence in R&D SEV-2015-0522, PlanNacional FIS2015-69258-P and MAT2017-88492-R, and Network FIS2016-81740-REDC), the Catalan AGAUR (2017SGR1369), Fundació Privada Cellex, Fundació Privada Mir-Puig, and Generalitat de Catalunya through the CERCA program. **Author contributions:** A.B., with the help of M.L., built the experiment, fabricated the samples, performed the measurements, and analyzed the data. A.B., R.Y., M.S., Y.S., and F.J.G.d.A. contributed to the theoretical modeling. M.L. and N.F.v.H. conceived the experiment. A.B. wrote the manuscript. All authors contributed to the interpretation of the data, discussion, and writing of the manuscript. **Competing interests:** The authors declare that they have no competing interests. **Data and materials availability:** All data needed to evaluate the conclusions in the paper are present in the paper and/or the Supplementary Materials. Additional data related to this paper may be requested from the authors.

Submitted 30 October 2018
Accepted 21 March 2019
Published 10 May 2019
10.1126/sciadv.aav8965

Citation: A. Block, M. Liebel, R. Yu, M. Spector, Y. Sivan, F. J. García de Abajo, N. F. van Hulst, Tracking ultrafast hot-electron diffusion in space and time by ultrafast thermomodulation microscopy. *Sci. Adv.* **5**, eaav8965 (2019).

Downloaded from http://advances.sciencemag.org/ on May 12, 2019

Science Advances

Tracking ultrafast hot-electron diffusion in space and time by ultrafast thermomodulation microscopy

A. Block, M. Liebel, R. Yu, M. Spector, Y. Sivan, F. J. García de Abajo and N. F. van Hulst

Sci Adv **5** (5), eaav8965.
DOI: 10.1126/sciadv.aav8965

ARTICLE TOOLS http://advances.sciencemag.org/content/5/5/eaav8965

SUPPLEMENTARY MATERIALS http://advances.sciencemag.org/content/suppl/2019/05/06/5.5.eaav8965.DC1

REFERENCES This article cites 49 articles, 3 of which you can access for free
http://advances.sciencemag.org/content/5/5/eaav8965#BIBL

PERMISSIONS http://www.sciencemag.org/help/reprints-and-permissions

Use of this article is subject to the Terms of Service

Science Advances (ISSN 2375-2548) is published by the American Association for the Advancement of Science, 1200 New York Avenue NW, Washington, DC 20005. 2017 © The Authors, some rights reserved; exclusive licensee American Association for the Advancement of Science. No claim to original U.S. Government Works. The title *Science Advances* is a registered trademark of AAAS.

Downloaded from http://advances.sciencemag.org/ on May 12, 2019